

THE SPEAR INSTRUMENT AND ON-ORBIT PERFORMANCE

JERRY EDELSTEIN¹, ERIC KORPELA¹, JOE ADOLFO¹, MARK BOWEN¹, MICHAEL FEUERSTEIN¹, JEFFREY HULL¹,
SHARON JELINSKY¹, KAORI NISHIKIDA¹, KEN MCKEE¹, PETER BERG¹, RAY CHUNG¹, JORG FISCHER¹,
KYOUNG-WOOK MIN², SEUNG-HAN OH², JIN-GUEN RHEE², KWANGSUN RYU², JONG-HO SHINN²,
WONYONG HAN³, HO JIN³, DAE-HEE LEE³, UK-WON NAM³, JANG-HYUN PARK³, KWANG-IL SEON³, IN-SOO YUK³

¹Space Sciences Laboratory, University of California, Berkeley, CA 94720

²Korea Advanced Institute of Science and Technology, Dajeon, Korea 305-701 and

³Korea Astronomy Observatory, Dajeon, Korea 305-348

Draft version February 5, 2008

ABSTRACT

The *SPEAR* (or “*FIMS*”) instrumentation has been used to conduct the first large-scale spectral mapping of diffuse cosmic far ultraviolet (FUV, 900-1750 Å) emission, including important diagnostics of interstellar hot (10^4 K – 10^6 K) and photoionized plasmas, H₂, and dust scattered starlight. The instrumentation’s performance has allowed for the unprecedented detection of astrophysical diffuse far UV emission lines. A spectral resolution of $\lambda/\delta\lambda \sim 550$ and an imaging resolution of 5’ is achieved on-orbit in the Short (900 – 1175 Å) and Long (1335 – 1750 Å) bandpass channels within their respective 7.4° x 4.3’ and 4.0° x 4.6’ fields of view. We describe the *SPEAR* imaging spectrographs, their performance, and the nature and handling of their data.

Subject headings: ultraviolet: ISM, instrumentation: spectrographs

1. INTRODUCTION

The Spectroscopy of Plasma Evolution from Astrophysical Radiation (hereafter *SPEAR* and *a.k.a.* “*FIMS*”) payload is surveying the sky for cosmic FUV emission. The *SPEAR* mission, launched 27 Sep. 2003, its science objectives, and the mission profile and performance are described in Edelstein et al. (2005). *SPEAR*’s bandpass ($\lambda\lambda$ 900 – 1750 Å), spectral resolution ($\lambda/\delta\lambda \sim 550$), large field of view (7.4° x 4.5’), and imaging resolution ($\sim 5'$) facilitate the measurement of energetic interstellar gas while rejecting air-glow emission and stellar contamination that have plagued earlier measurements attempts. This paper describes the *SPEAR* instrument, its on-orbit performance, and the basic processing of instrument data. Measurements of faint diffuse FUV emission lines are a difficult undertaking wherein instrumental and systematic errors can dominate the results. Therefore, we discuss instrumental facets in detail in order to allow users to understand the nature and quality of *SPEAR* data. Further technical description regarding various aspects of the *SPEAR* instrument are found in the literature (Edelstein et al. 2003; Korpela et al. 2003; Nam et al. 2003, 2002; Ryu et al. 2003).

2. THE SPECTROGRAPHIC METHOD

The *SPEAR* instrument consists of dual imaging spectrographs optimized for the detection of faint diffuse FUV radiation. The two spectral channels are designated as the “Short” ($\lambda\lambda$ 900 – 1175 Å) and “Long” ($\lambda\lambda$ 1335 – 1750 Å) bandpasses. The bands were chosen to include astrophysically important emission lines from abundant ionic species while avoiding instrumental contamination by the intense H I λ 1216 Å and O I λ 1304 Å geocoronal radiation. Each channel uses an optical configuration (see Fig. 1) consisting of a collecting mirror, a slit, a diffraction grating, and a detector. The unique two-element f/2.2 optical system has an off-axis

parabolic-cylinder collecting mirror that focuses plane-parallel light to a slit. Cylindrical radiation from the slit then strikes a constant-ruled grating with an elliptical figure that corrects on-axis aberrations to the third order. Diffracted light is imaged as a spectrum on a planar position sensitive photon counting detector. Radiation from off-plane angles is imaged along the detector perpendicular to the dispersion plane, analogous to a slit-imaging spectrograph. The cylindrical-source scheme doubles the usable imaging angle in comparison with classical point-source spectrographs. The result is a large solid angle – collecting area product, a determining factor for diffuse source sensitivity. The design is an extension of the *EURD* instrument (Bowyer et al. 1997)

Diffuse FUV spectrograph performance is a function of optical quality, dispersion, efficiency, and scattering due to surface or grating imperfections. The collecting mirrors were measured to have a focal line width of $< 100 \mu\text{m}$ FWHM at the focal distance of 15 cm and a surface roughness of 10 Å RMS. The gratings were polished to $< 35 \text{ Å}$ RMS surface roughness and holographically ruled with a blazed profile formed by ion-beam ablation of chemically etched grooves, providing 65% peak groove diffraction efficiency. The Long and Short channels (hereafter referred to as “L/S”) use the same grating figure while the Long channel works in first order at 3000 line mm^{-1} and the Short channel works in second order at 2250 line mm^{-1} . The L/S optics use coatings, MgF₂ on Al and B₄C on a thin Cr base (Keski-Kuha et al. 1995), were chosen to optimize bandpass efficiency and resist degradation by atomic oxygen.

Care was taken to reduce background noise from strong airglow lines, stars, detector and ion background, and optics fluorescence. The Long channel includes a flexure-mounted, zero-power CaF₂ cylindrical meniscus filter that excludes geocoronal Lyman α before the 150 μm slit. The Long band response is limited at short λ by the CaF₂ filter and at long λ by the detector photocathode

(see below) such that high-order diffraction is rejected. The Short band is un-filtered and its response is limited by falling optical coating and diffraction efficiency at short λ , and by the detector photocathode at long λ , although high-order response to the bright He I λ 537 is found in flight data. The Short channel uses MgF_2 windows that transmit $\lambda > 1150 \text{ \AA}$ to detector areas adjacent to the science field so that instrumentally scattered Lyman α airglow can be monitored. Consequently, the L/S science fields of view are $7.4^\circ \times 4.3'$ and $4.0^\circ \times 4.6'$. We estimate the radiation induced filter fluorescence from the filters' fluorescence rate due to a predicted orbital radiation environment, the detector's sensitivity to the fluorescence spectrum, and the detector's view of the filters. The shutter can be selected to admit 0%, 1%, 10% or 100 % of the available light for safe and photometric observations of bright sources.

2.1. Sensor and Systems

Each channel's spectrum is focused upon a separate position-sensitive photon-counting microchannel plate (MCP) Z-stack that is top coated with an L/S optimized photocathode of CsI and KBr. The stacks' 23mm square active fields share a single event position encoding system by using a unique cross delay-line anode (Rhee et al. 2002) with a bifurcated line to sense the spectral axis and a continuous line to sense the imaging axis. The anode axes are rotated 15° with respect to the dispersion plane to mitigate the appearance of false spectral features from anode or electronics differential non-linearity. Event axes positions are independently determined by precisely timing the arrival times of amplified anode pulses. The position conversion system has a fixed dead-time of $86 \mu\text{s}$ per event. A stimulation unit injects an artificial event signal for each field corner at 10 Hz so that thermal drifts in the position encoding system can be calibrated in flight. The amplifiers also produce a signal proportional to every event's charge amplitude to allow for the rejection of low amplitude noise or high amplitude ion and cosmic ray events. A count-rate monitor turns off the detector in case of excessive count-rates. Observation restart is automatically attempted within 2 to 30 s so that entire survey sweeps will not be lost to momentary bright stars transits. Timing marks are inserted into the data stream to accurately account for such interruptions.

The spectrographs are contained in an enclosure including the gratings, order baffling, the detector, a shutter-slit unit, a mirror unit with field baffling, and a deployable dust cover. Each channel is optically baffled from the other. Thermal ion detector noise is suppressed by positively biased wire grids and baffles on all enclosure openings and the detector face, and by high-energy magnets at the slit. The $5 \times 8 \text{ cm}$ optics are bonded to thermally-matched metal flexures using a low-modulus adhesive, and then attached to three-point mounts. The gratings were aligned with divergent FUV radiation illuminating the slit and mirror-slit alignment used visible collimated light. Full-system ground calibration with collimated FUV light established the field width and angular scale. The complete 22 kg instrument is $45 \times 45 \times 15.5 \text{ cm}$ in size.

The instrument uses ground command to set payload operating modes and to tune critical engineering parameters such as detector voltage levels, detector electronics

thresholds, and shutter timing. On-board software controls the instrument operation, data packetization and flow, and spacecraft-time synchronization. Commands can synchronize the instrument and spacecraft clocks to 250 ms. Detector events (photons, stimulation events, noise events) are queued into packets interleaved with a 10 Hz time reference and other marks used during data reduction for attitude synchronization. Science data are retransmitted to a mass memory system at 200 kbps for downlink. The data system throughput impacts the event rate resulting in a net dead-time of $\sim 133 \mu\text{s}$ per event, corresponding to a throughput loss of 5% for a 1kHz event rate. Dead-time was determined by on-orbit observations of identical bright sky regions using the 10% and 100% shutter positions.

3. PHOTON EVENT PROCESSING AND CALIBRATION

Individual photon data events are subject to automatic processing in-orbit and to ground-based pipeline processing. Photon events are selected for a valid pulse height based upon the nominal distribution (65% FWHM). Low-amplitude noise events are discarded by the on-board electronics. Typically, $\sim 7\%$ of telemetered events, presumably caused by ions and cosmic rays, are discarded due to excessive pulse amplitude. Photon events are marked with the concurrent total count rate so that dead-time corrections can be calculated. Photon detector coordinates are pipeline corrected for detector electronics thermal drift and distortion every 5 s using a 2-d gradient distortion referenced to the stimulation marks' centroids. The drift correction, almost entirely in the dispersion direction, decays from $\sim 0.6 \text{ \AA}$ to insignificance within 120 s of an observation's start. The stim centroid positions are stable to $\sim 0.15 \text{ \AA}$. Photon events occurring outside of an active boundary, defined using deep detector exposures, are rejected including a $1 - 10 \text{ s}^{-1}$ event "warm-spot" near the Long channel's detector edge. Other photon data integrity checks reject $< 0.5\%$ of the data.

Photon wavelength, λ , and field angle, ϕ , are derived from detector coordinates using simple polynomial plate scales in the spectral and angular dimensions. The imaging angular scale, $0.31^\circ \text{ mm}^{-1}$, was measured pre-flight using a collimated FUV spectral illumination at precise field angles. Imaging L/S angular resolution, averaged over the bandpass, was measured from bright-star crossings and are $6.5'$ and $4.5'$ HEW. The L/S spectral dispersion scales, 17.9 \AA mm^{-1} and 12.0 \AA mm^{-1} , were determined by comparing the Gaussian-fit centroids of measured auroral emission lines to centroids derived from predicted air-glow emissions (Strickland et al. 1999) that have been smoothed by a 2 \AA HEW Gaussian.

A λ distortion correction was constructed using composite emission line spectra from 20 orbits of auroral observation. The L/S central λ error correction for each of 15 and 9 lines was determined at $45'$ intervals. The correction applies a 2-d gradient to λ and ϕ with a residual angle-integrated line λ centroid error of 0.5 \AA and 0.75 \AA . The resulting spectra shows remaining higher order distortions. Consequently, a second λ correction was constructed using composite line spectra from 155 orbits of auroral observations. The L/S λ error-correction for 22 and 15 lines was determined in $5'$ angular steps and then boxcar smoothed at $15'$ angular width. Corrections for λ 's between the measured lines were estimated by

a low-tension spline fit. The second correction improves spectral resolution and centroid accuracy, but introduces flat-field non-linearity as described below. The result is an L/S angle-integrated median λ centroid errors of 0.11\AA and 0.081\AA , with mean errors of $0.24 \pm 0.41\text{\AA}$ and $0.21 \pm 0.24\text{\AA}$. Residual systematic errors of $\sim 1\text{\AA}$ which we intend to correct in future work, persist in the S channel for $\lambda < 1000\text{\AA}$.

Spectral resolution is measured from the observed auroral spectra, together with airglow spectra for the S channel, after applying the distortion corrections. Because the sources are diffuse, the results are independent of spacecraft pointing knowledge. The first correction gives an L/S spectral half-energy line width, averaged over the angular field, of 3.2\AA and 1.9\AA while the second correction widths are $2.95 \pm 0.76\text{\AA}$ and $1.71 \pm 0.33\text{\AA}$. These values are upper limits to the resolution because any intrinsic width of multiplets in the source spectra were not accounted.

Detector differential non-linearity (DNL) arises from the λ correction process from its application to distributed noise sources such as intrinsic detector noise, events from ions and penetrating cosmic rays, or instrumentally scattered airglow lines, a significant noise source in the Short channel. The processing-induced DNL can be corrected and eliminated if the distributed noise spectra is known because the DNL is fixed in detector coordinate space. Whether *uncorrected* DNL can charade as a spectral feature depends on the relative intensity of the distributed noise to the true external signal and on whether both the DNL and the feature have similar spectral profiles. We use simulations of the induced DNL by processing a uniform random distribution of photons on the detector to estimate that completely uncorrected DNL can appear as line emission features with an intensity of $\sim 1.5\%$ of the distributed noise level.

An on-orbit 'dark' background integration of events due to intrinsic detector, particle and penetrating radiation noise was accumulated in 42 ksec from 250 orbits that include 0% shutter observations which were confirmed to exclude occasional mis-positioned shutter airglow leaks. The detector dark background rate is from $0.02\text{--}0.04\text{ counts s}^{-1}\text{\AA}^{-1}$ over the full science field angular height. The dark background shows the expected λ correction DNL features. In the S channel, instrumentally-scattered Lyman α 1216\AA airglow radiation is a significant contributor to the intrinsic background. The S channel scattering function, measured by comparing integrated closed-slit and open-slit background observations, is well fit by an exponential with 190\AA width and an intensity of $0.016\text{ counts s}^{-1}\text{\AA}^{-1}$ at the band center. The airglow correction can be estimated for observations subject to time-variable airglow by using the Short channel MgF₂ filter regions to measure the relative intensity of scattered Lyman α radiation.

4. SENSITIVITY CALIBRATION

The sensitivity to diffuse radiation is determined by the grasp, Γ , a product of the solid-angle, Ω , and effective area, A_{eff} . The solid angle for L/S, a product of the slit's angular width and the viewed angle per λ , constrained by the detector boundary, are $1.6 \times 10^{-4}\text{ sr}$ and $8.4 \times 10^{-5}\text{ sr}$, respectively. The A_{eff} was determined using special calibration observations where repetitive roll-sweeps of the

$4.5'$ field of view crossed a star, and using regular sky-survey operations. Data were acquired over a range of field-angle positions on the detector for both cases. For the calibration data, a 'timed-sweep' method was used to derive star exposure times by dividing the spacecraft roll rate by the ground-calibrated angular slit width. About 15% of the sweeps were rejected due to data faults. The net stellar signal was determined after subtracting adjacent sky background ($\sim 5\text{--}10\%$ of the stellar flux). The sweeps' stellar count rates show a nearly Gaussian distribution with a $\sim 15\%$ width. For the sky-survey data, we used the sky mapping method (Edelstein et al. 2005) to obtain source and background spectra of the field stars. The sky-map derived flux was verified to reproduce the more comprehensive timed-sweep calibration results to within 10–15%.

For the L channel, calibration observations of G191B2B and HD188665 provided 253 s and 19 s of stellar exposure, and 13.2 k and 26.1 k photons (background subtracted) for comparison to the spectra of Kruk et al. (1995) and Buss et al. (1995), respectively. The field stars HD 74753, HD 74273, and HD 72014 were mapped and referenced to their *IUE* spectra. The A_{eff} for each star was derived by dividing the observed count rate by the reference flux, with a typical statistical error per 1.5\AA spectral bin of $\sim 10\%$. The stars' A_{eff} were averaged using inverse counting-error weighting and fit with a third-order polynomial to obtain the spectral calibration curve, shown in Fig. 2. The individual star's A_{eff} deviate from the weighted average by $\sim 20\text{--}30\%$ over the band with no discernible in-flight time trend. At the L band center, we find $A_{eff} = 0.20\text{ cm}^2$, corresponding to a full-field grasp of $\Gamma = 3.2 \times 10^{-5}\text{ cm}^2\text{sr}^{-1}$.

For the S channel, a calibration observation of HD 93521, conducted March to April 2004, provided 146 s and 9300 photons (background subtracted) for comparison to the spectra of Buss et al. (1995). Also, the field star HD 1337 was observed in the survey during November 2003 for 57 sec with 3500 counts and referenced to its *HUT* spectra. Each stars' A_{eff} was derived using eight λ 10–30 bins that avoid the airglow Lyman series and have $\lesssim 6\%$ statistical error, except for the λ 915–925 bin with a 37% error. The A_{eff} bins were fit with a second-order polynomial to obtain spectral calibration curves, shown in Fig. 2. At the S band center we find that $A_{eff} = 0.035\text{ cm}^2$ for HD 1337, and $A_{eff} = 0.016\text{ cm}^2$ for HD 93521. There appears to be a significant S-channel degradation with time. The earlier A_{eff} corresponds to a full-field height S grasp of $3.0 \times 10^{-6}\text{ cm}^2\text{sr}^{-1}$. HD 1337 (AO Cas) is an eclipsing binary with a 3.4 day period and a $\sim \pm 7.5\%$ photometric variation in FUV resonance lines, such as NV $\lambda\lambda$ 1240 and CIV $\lambda\lambda$ 1550 (Gies & Wiggs 1991). Our measurement of AO Cas should be of a mean intensity because it broadly samples the binary phase in λ bins that are large compared to observed phased velocity shifts. We intend to refine our sensitivity calibration and its temporal behavior in future work by measuring more stars.

Systematic errors in the determination of exposure times and in the reference stellar spectra are likely to dominate our flux calibration accuracy. We estimate these errors systematic overall to be $\sim 25\%$. The relative angular sensitivity variation from the mean response is

6.5% as found from the off-axis response to bright in-band telluric diffuse night glow emission lines (e.g. O I 1356Å, H I 1026Å) accumulated over all observations. We presume that the night glow lines are effectively constant in intensity over the sky because these data are taken over a wide range of zenith angles. Compared to its pre-launch performance, *SPEAR's* on-orbit sensitivity was unfortunately degraded from its delivered performance due to contamination caused by spacecraft and launch ground operations.

5. CONCLUSION: PERFORMANCE

SPEAR's sensitivity can be estimated from the on-orbit performance values. The ultimate capability to detect diffuse emission with *SPEAR* depends on mission factors such as sky exposure, attitude knowledge and background temporal behavior. These factors are treated elsewhere in this issue (Edelstein et al. 2005). We find that the dominant cause of background is a combination of detector dark noise and instrumentally scattered airglow for the Short channel, and dark noise and interstellar continuum for the Long channel. In-orbit measured L/S background rates have typical values of ~ 0.02 counts $s^{-1} \text{ \AA}^{-1}$ for diffuse high latitude sky fields (excluding stars). These values correspond to an L/S isolated emis-

sion line $3\text{-}\sigma$ sensitivity of 55 and 750 photons $s^{-1} \text{ cm}^{-2} \text{ sr}^{-1}$ for diffuse illumination filling the full angular field, presuming a 10 ksec observation, and a background determination over 100Å of bandpass.

Limits to the measurement of emission lines that are not fully isolated from airglow lines, such as OVI 1032 Å near Lyman β 1027 Å and CIII 977 Å near Lyman γ 972 Å, depends on the intensity of the airglow line and the accuracy of spectral profiling used in compound spectral line-fit modeling. We leave a systematic treatment of such modeling and its limitations to papers specifically observing these spectral lines. As an example of the sensitivity, however, we provide that 7000 LU of OVI λ 1032 was measured with 5σ significance in a 31 ks observations toward the Eridanus Loop (Kregenow et al. 2005).

SPEAR / FIMS is a joint project of KASI & KAIST (Korea) and U.C., Berkeley (USA), funded by the Korea MOST and NASA Grant NAG5-5355. We thank the team for their dedication in producing the instrument, and Jerry thanks Liz and Dan for immeasurable contributions.

REFERENCES

- Bowyer, S., Edelstein, J., & Lampton, M. 1997, ApJ, 485, 523
 Buss, R. H., Kruk, J. W., & Ferguson, H. C. 1995, ApJ, 454, L55+
 Edelstein, J. et al. 2003, Proc. SPIE, 4854, 329
 —. 2005, ApJ, this issue
 Gies, D. R. & Wiggs, M. S. 1991, ApJ, 375, 321
 Keski-Kuha, R. A., Osantowski, J. F., Blumenstock, G. M., et al. 1995, Proc. SPIE, 2428, 294
 Korpela, E. J. et al. 2003, Proc. SPIE, 4854, 665
 Kregenow, J. et al. 2005, ApJ, this issue
 Kruk, J. W., Durrance, S. T., Kriss, G. A., Davidsen, A. F., Blair, W. P., Espey, B. R., & Finley, D. S. 1995, ApJ, 454, L1+
 Nam, U. et al. 2003, Proc. SPIE, 4854, 602
 Nam, U.-W. et al. 2002, Journal of Astronomy and Space Sciences, 19, 273
 Rhee, J. G. et al. 2002, Journal of Astronomy and Space Sciences, 19, 57
 Ryu, K. et al. 2003, Proc. SPIE, 4854, 457
 Strickland, D. et al. 1999, J. Quant. Spectrosc. Radiat. Transf., 62, 689

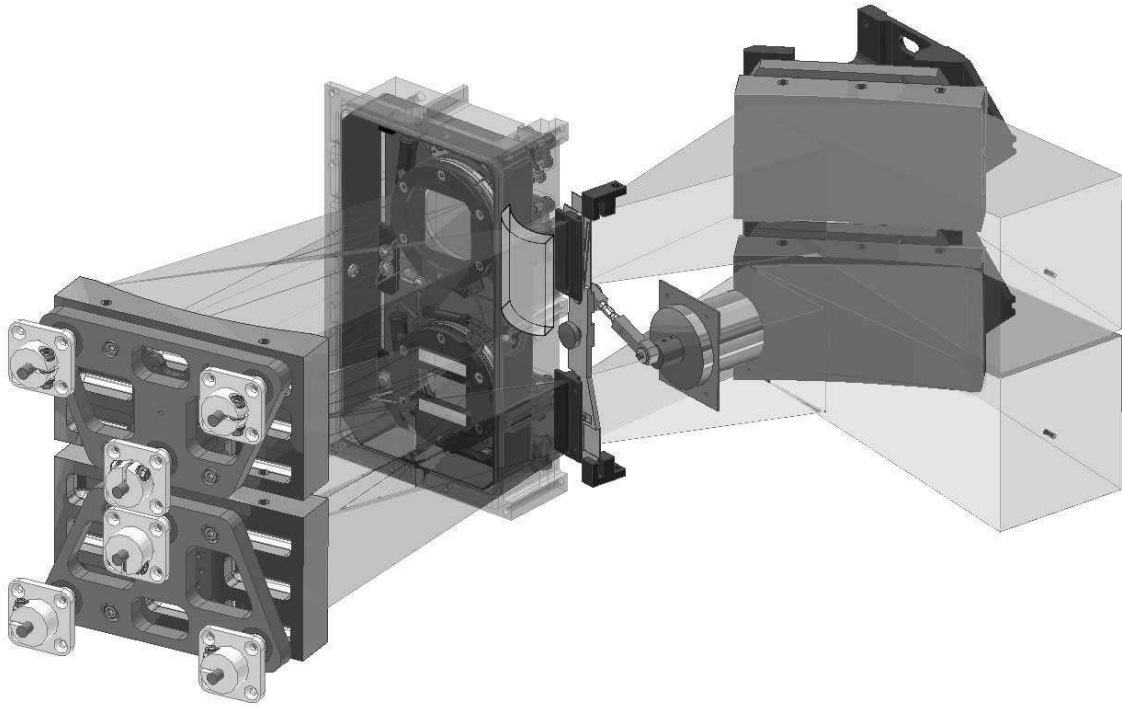


FIG. 1.— The *SPEAR* dual-spectrograph optical layout. Light is collected by the mirrors (*right*) to a motorized slit shutter. The Long channel (*upper*) is filtered by a CaF_2 meniscus after the slit. The light then diffracts from gratings (*left*) to photon counting detectors. The Short channel (*lower*) is un-filtered, although MgF_2 windows on the detector abut the science field to monitor airglow. For scale, the grating is ~ 8 cm long.

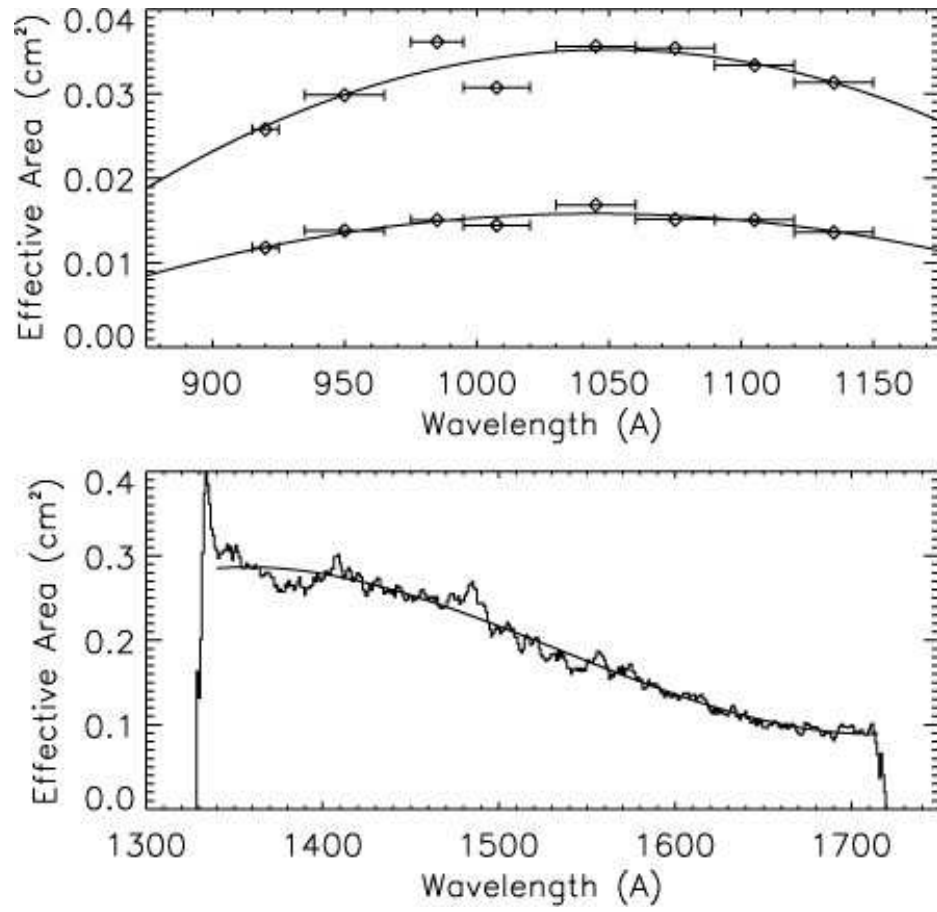


FIG. 2.— The *SPEAR* A_{eff} calibration fit to stellar observations for (*top panel*) the Short band in November 2003 (*upper curve*) and April 2004 (*lower curve*), and for the Long band (*bottom panel*) fit to the average histogram from five stellar observations.